ADVANCED FUNCTIONAL MATERIALS
www.afm-journal.de

From Mechanics to Electronics: Influence of ALD Interlayers on the Multiaxial Electro-Mechanical Behavior of Metal–Oxide Bilayers

*Johanna Byloff, Vivek Devulapalli, Daniele Casari, Thomas E. J. Edwards, Claus O. W. Trost, Megan J. Cordill, Shuhel Altaf Husain, Pierre-Olivier Renault, Damien Faurie, and Barbara Putz**

The applicability of metal-polymer thin films in flexible electronics and space applications is fundamentally limited by the trade-off between mechanical and functional performance. This study shows how atomic layer deposited (ALD) amorphous AlO_xH_y interlayers (0–25 nm) directly control the electro-mechanical functionality of sputter-deposited aluminum films on polyimide substrates. Using uni- and equi-biaxial tensile testing with in situ XRD and electrical resistance measurements, it is demonstrated that interlayer thickness determines both deformation mechanisms and electrical strain limits. Adding an ALD layer between the polymer substrate and the metal thin film significantly improves the deformability of the system. While a single ALD cycle enhances ductility, surprisingly a 1 nm AlO_xH_y interlayer causes early electrical failure. Optimal performance—improved ductility, delayed cracking, and maintained electrical conductivity under large deformation—is achieved at 5–10 nm interlayer thickness. Beyond this range, embrittlement causes early electrical failure through oxide-initiated cracking. The work establishes quantitative design rules linking the nanoscale interface structure to macroscale electro-mechanical performance, enabling flexible electronics with tailored mechanical properties and enhanced electrical functionality. These findings provide a direct pathway from fundamental interface engineering to high-performance flexible devices operating under multi-axial deformation.

1. Introduction

Thin metal films on polymer substrates are critical components in flexible electronics and space technology applications. In microelectronics, polyimide dielectrics separate metal wires and vias for multilayer interconnect packaging,[1] while in space applications, aluminum-polyimide systems are essential for high-precision instruments like the James Webb Space Telescope's sun shield subsystem[2] and X-ray detector optical blocking filters.[3] The combination of polyimide's excellent adhesion with aluminum[4] and good thermal stability up to 400 °C[5] together with aluminum's conductivity, reflectivity, and cost-effectiveness[6] makes the aluminum-polyimide system highly attractive for these demanding applications. However, mechanical reliability remains a significant engineering challenge due to potential mechanical failure on the basis of film cracking or interfacial delamination, which can compromise functional performance and operational lifetime.[7]

J. Byloff, V. Devulapalli, D. Casari, T. E. J. Edwards, B. Putz
Empa, Swiss Federal Laboratories for Materials Science and Technology
Laboratory for Mechanics of Materials and Nanostructures
Feuerwerkerstrasse 39, Thun 3602, Switzerland
E-mail: barbara.putz@empa.ch

J. Byloff
Laboratory for Nanometallurgy
ETH Zurich
Vladimir-Prelog-Weg 5, Zurich 8093, Switzerland

The ORCID identification number(s) for the author(s) of this article can be found under https://doi.org/10.1002/adfm.202526343

DOI: 10.1002/adfm.202526343

T. E. J. Edwards
Research Center for Structural Materials
National Institute for Materials Science
1-2-1 Sengen, Tsukuba 305-0047, Japan

C. O. W. Trost, M. J. Cordill
Erich Schmid Institute of Materials Science
Austrian Academy of Sciences
Jahnstrasse 12, Leoben 8700, Austria

M. J. Cordill, B. Putz
Department of Materials Science
University of Leoben
Franz Josef Strasse 18, Leoben 8700, Austria

S. Altaf Husain, P.-O. Renault
Institut Pprime
CNRS – Universite de Poitiers
11 Bd Pierre et Marie Curie, Poitiers 86073, France

Metallic adhesion-promoting interlayers (Cr, Mo, W, Ta) are known to induce stress concentrations that cause fragmentation at low strains and lead to early system failure during monotonic straining.[8–12] Similar limitations are observed in fatigue testing,[13] even though the resulting bilayer structures (e.g. Au / Cr) may exhibit deformation mechanisms that benefit their fatigue resistance: dislocation structures in the Au layer that evolve into a geometrically necessary boundary parallel to the Cr-Au interface impede further dislocation motion during cyclic in situ TEM experiments.[14] Alternatively, we recently (2025) demonstrated the use of a thin amorphous atomic layer deposited (ALD)-oxide as an interlayer (IL) for flexible applications,[15] inspired by intermixing reactions at the metal-polymer interface.[16] A 5 nm-thick ALD-AlO_xH_y interlayer facilitates ductility in the metal film (Al) by enabling dislocation activity and localized plastic deformation.[15] In addition to mechanical robustness, functional properties can also benefit, as demonstrated by improved electrical characteristics of flexible thin film transistors when adding a 20 nm-thick amorphous Al_2O_3 IL.[17] Furthermore, atomic-scale interface design has been shown to improve mechanical bonding and conversion efficiency in thermoelectric devices.[18]

To establish design principles for flexible metal/ALD-oxide bilayers and to reveal the deformation mechanisms governing metal-oxide interfaces, we systematically varied ALD interlayer thickness (0.14–25 nm) and investigated the electro-mechanical response of Al-AlO_xH_y bilayers under different loading conditions. Thin amorphous ALD-oxides can be extremely strong and ductile provided they are defect-free. Limiting factors for lowering of defect content are layer thickness (number of ALD cycles/growth per cycle) or H content (deposition conditions).[19] For ALD-alumina, the identified thickness limit for brittle cracking in Al/AlO_xH_y nanolaminate and multilayer architectures is greater than or equal to 5 nm at a H content of 10.1 at%.[20–22] Next to the polymer substrate, H content in the interlayer up to 27.5 at% can be supported without embrittlement at 5 nm thickness.[15]

In view of flexible applications, multiaxial mechanical characterization of metal-ceramic bilayers is needed to evaluate the anisotropic deformation properties of materials under different loading ratios.[23–25] Thin metal films on polymer substrates (50 nm Ni,[26] 50–150 nm Al[21]) are stronger in equi-biaxial tension compared to uniaxial tensile loading. For ceramics, on the other hand, load multiaxiality affects mechanical strength typically negatively (crystalline,[27] and amorphous[28,29] examples). In a previous work,[21] the observed weakening of Al layers in Al/ALD-alumina multilayers under biaxial loading (which exhibit strengthening in uniaxial tension) is attributed to biaxial weakening of AlO_xH_y (H content 10.1 at%) within the multilayers. Given the important role of layer order and proximity to the polymer substrate on the strength of flexible thin films,[30] this behavior might not translate to bilayer films with ALD interlayers.

In this work, we report uni- and equi-biaxial tensile testing with in situ X-ray diffraction (XRD), electrical resistance measurements[31–35] and post-mortem lateral and through thickness fragmentation analysis of crystalline Al films (150 nm) with amorphous ALD-oxide interlayers (0.14–25 nm thickness) on flexible polymer substrates (50 µm thickness). Bilayers are fabricated using a unique ALD-physical vapor deposition (PVD) cluster setup with in-vacuo transfer capability (**Figure 1**, for a more detailed schematic, see[15]). We demonstrate that the addition of an ALD layer between the polymer substrate and the metal thin film significantly improves the electrical performance of the Al layer and the deformability of the whole system. Through in situ XRD and peak broadening, it is possible to describe deformation domains in crystalline Al layers.[36] Combining uni- and equi- biaxial loading, the complete biaxial stress dependence of plasticity can be assessed.[37] These findings are compared to different thin film mechanics models and placed in context with length-scale dependent deformation behavior observed in other bi- and multilayer architectures on flexible polymer substrates, demonstrating how interlayer thickness governs the transition between ductile and brittle deformation regimes. We establish a framework describing mechanical behavior as a function of interlayer thickness, enabling the rational design of flexible thin films with tailorable properties and high interface quality.

2. Results

2.1. Structural Characterization

We use transmission electron microscopy (TEM) and precession electron diffraction (PED) orientation mapping to investigate whether the subsequently measured mechanical properties depend on the film microstructure. **Figure 2** presents cross-sectional overview bright field (BF) TEM micrographs and inverse pole figure (IPF-z) maps acquired in the out-of-plane direction. For this analysis, focused ion beam (FIB) lift-out lamellae were prepared from bilayer systems consisting of Al with an amorphous interlayer (IL) deposited on a polyimide substrate. As the interlayer is amorphous, only the Al layer can be seen in the PED orientation maps. All Al films exhibit a uniform thickness and grain size (reported in Table S2, Supporting Information). The majority of grains are columnar and show no preferred crystallographic orientation. In-plane orientation maps (Figure S1, Supporting Information) confirm the absence of texture. For the 25 nm IL system, the interlayer is clearly visible in the TEM cross-section (Figure 2F i). At lower IL thicknesses (e.g. 1 nm), its visibility is reduced as a result of substrate roughness and the finite lamella thickness. Additionally, the beam-sensitive polyimide substrate suffered damage during FIB preparation and TEM imaging, as evident in Figure 2D,E.

2.2. Uniaxial tensile testing

Figure 3A–F shows the evolution of the stress in the Al layer (Al (111) Bragg peak) in the axial (σ_x, black) and transverse (σ_y, grey) direction during uniaxial tensile testing as a function of ALD interlayer thickness. All experiments presented here use a constant polymer thickness of 50 µm. Residual stresses (green symbols Figure 3) were measured before straining. Differences

S. Altaf Husain, D. Faurie
LSPM-CNRS, UPR3407
Universite Sorbonne Paris Nord
99 Avenue Jean-Baptiste Clement, Villetaneuse 93430, France

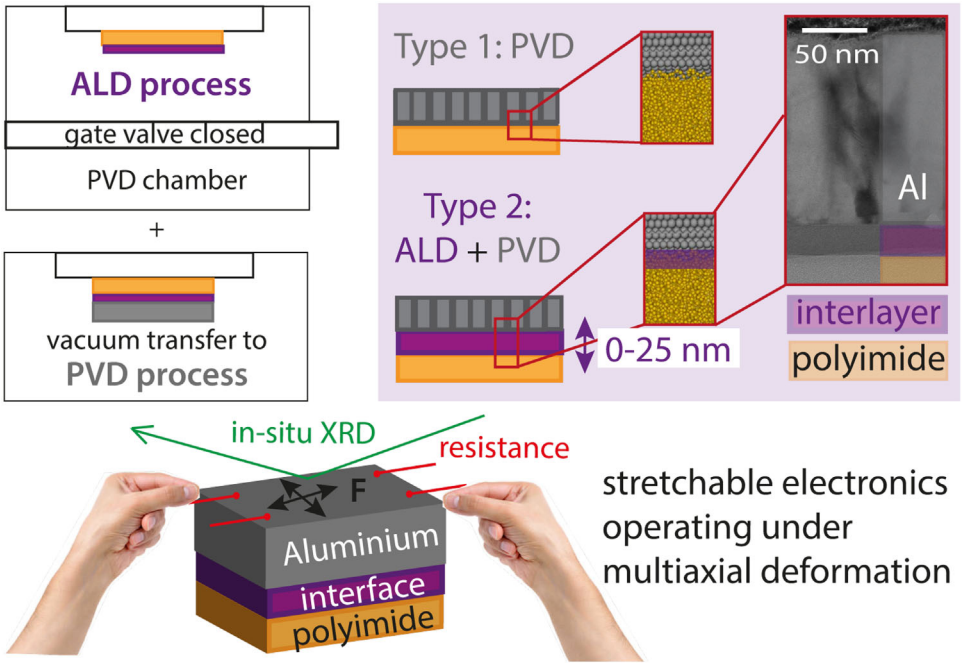

Figure 1. Overview of the synthesis process, sample design and characterization. Samples were produced in a combined ALD-PVD chamber, where the ALD interlayer (IL) thickness was varied from 0 to 25 nm (0, 0.14, 1, 5, 10, and 25 nm thicknesses). All IL systems were strained uni- and biaxially with in situ XRD and resistance measurements.

in axial and transverse values result from sample pre-loading to ensure a flat film at the beginning of the tensile test. Full width half maximum (FWHM) evolution corresponding to axial measurements is given below each graph. FWHM evolution can indicate changes in deformation behavior if the size of the diffraction domains (e.g. grains) stays constant. Changes in deformation behavior are, for example, a change from the elastic to plastic regime due to a substantial increase in strain heterogeneities.[30] It is important to note that uniaxial tensile testing of polymer-supported films usually results in a biaxial stress state in the metal thin film due to a difference in Poisson's ratio ($\Delta\nu$ between film and substrate). From the two correlative datasets, mechanical deformation characteristics equivalent to fracture or yield stresses can be derived in the loading direction,[38] while transverse measurements reveal delamination phenomena.[39] A deviation from the linear stress-strain response in the axial direction together with an increase in FWHM was used to determine 0.2% yield stresses (marked with red crosses). The corresponding evolution of transverse FWHM, which shows a similar trend to axial FWHM, is provided as Figure S2 (Supporting Information). No XRD signal is obtained from the ALD interlayers due to their limited thickness and amorphous structure. Additionally, the normalized recorded electrical resistance R/R_0 is shown in Figure 3A–F as a function of applied engineering strain ε_x (dashed orange lines). It is expected to increase according to $R/R_0 = L/L_0 = (1+\varepsilon_x)^2$ (solid orange line, gauge length L_0 and initial length L_0[40]) during loading until deviation (crack onset strain, COS) due to film failure, either caused by necking-like damage or cracking. Characteristic values derived from Figure 3 are summarized in Table S3 (Supporting Information) as a function of interlayer thickness.

The results of the uniaxial tensile testing campaign provide insights into how the ALD interlayer thickness affects both the onset of plastic deformation and subsequent failure mechanisms. By correlating stress evolution with peak broadening and changes in electrical resistance, we can distinguish between systems that fail due to brittle fracture versus those that accommodate strain through ductile mechanisms.

It is evident from Figure 3A,C,E that Al films with 0, 1, and 25 nm ALD interlayer exhibit a stress-strain behavior characteristic for through-thickness cracking and brittle deformation: a pronounced peak in the axial (black) stress–strain curve at ≈2% strain (crack initiation) followed by rapid relaxation of tensile stresses before reaching a stress plateau, which can be attributed to an overlap of stress relaxation zones at the crack edges.[41] Correspondingly, the normalized electrical resistance deviates early as through-thickness cracks start to form (low COS values), and increases rapidly as the number of percolation paths for electrons in the film is reduced (large $R/R_{0,max}$ values, 2.5–3). Within the three brittle film systems, the Al film with 1 nm ALD interlayer exhibits the highest yield and ultimate tensile strength in the axial direction (660 ± 23 MPa, see Table S3 in Supporting Information for a complete list of values), a higher plateau stress (ca. 400 MPa compared to 200 MPa for 0 and 25 nm), and lower $R/R_{0,max}$, while only the film with 25 nm interlayer exhibits a noticeably higher COS. All films exhibit a narrow strain range from yield to crack onset, with this region being virtually absent in the 1 nm film. Upon unloading, all brittle systems experience an initial drop due to load reversal, followed by a linear stress regime and stress plateau.

Conversely, the Al films with 0.14, 5, and 10 nm ALD interlayer exhibit more ductile stress-strain behavior with a

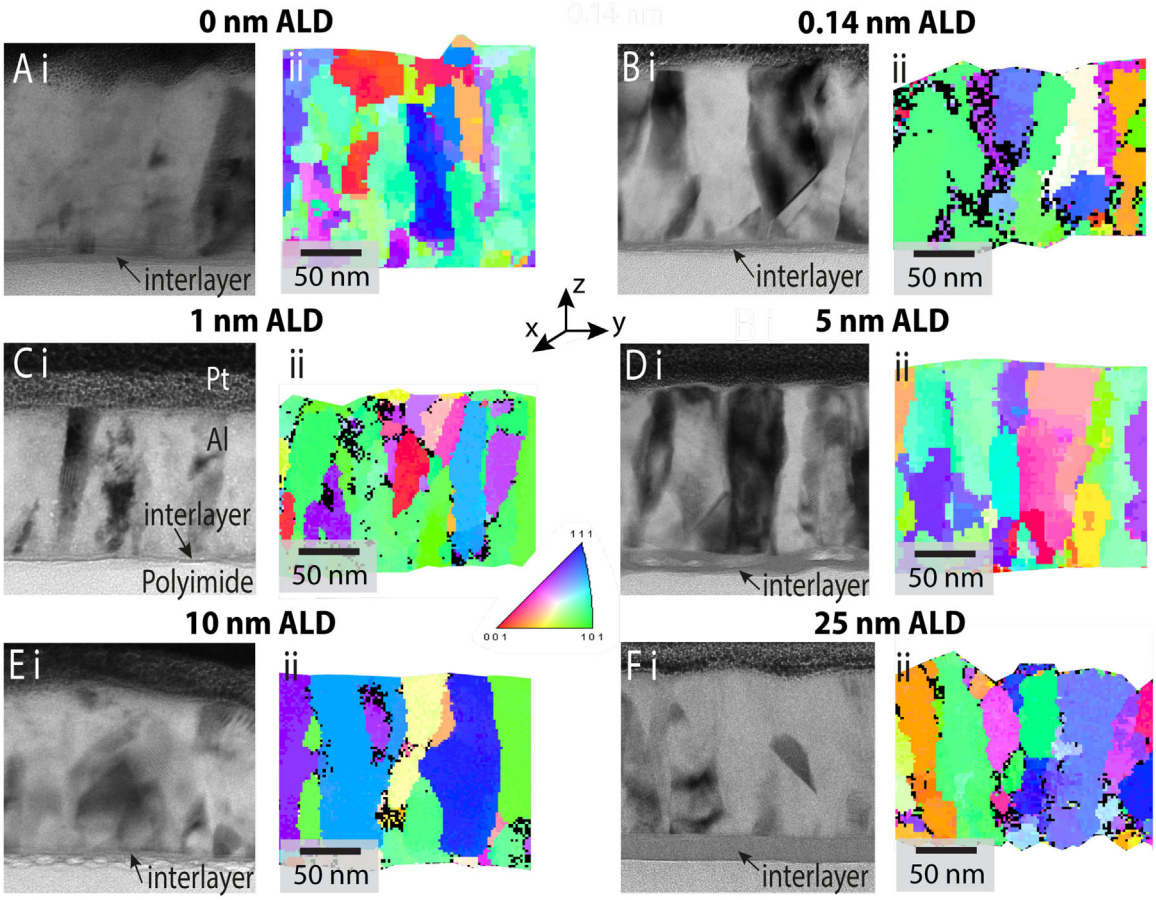

Figure 2. Cross-sectional TEM images (i) and precession electron diffraction (PED) orientation maps (ii) of Al/polyimide bilayer systems. A) Al/PI reference system without ALD interlayer. B) 0.14 nm ALD interlayer. C) 1 nm ALD interlayer. D) 5 nm ALD interlayer. E) 10 nm ALD interlayer. F) 25 nm ALD interlayer. The wavy interfaces in panels B i, D i, and E i result from damage to the beam-sensitive polyimide substrate during FIB sample preparation and TEM imaging. Orientation maps were acquired in the out-of-plane direction; only the crystalline Al layer is displayed, as the ALD interlayers are amorphous.

plateau-like stress evolution as necks (local thinning) progressively develop after reaching the maximum strength, $\sigma_{x_{max}}$ (highest value in Figure 3B,D,F). Additionally, maximum stresses are reached at higher strain values after yielding. Determination of $\sigma_{x_{max}}$ is facilitated through correlation of axial and transverse datasets (good alignment between $\sigma_{x_{max}}$ and $\sigma_{y_{max}}$). Within the sample series, the Al film with 5 nm IL can sustain the highest applied strains before reaching $\sigma_{x_{max}}$. As a result of enhanced ductility and local plastic deformation (necking) in all films, the COS values are shifted to ≈6% applied strain, where an electrically critical neck density has formed, and $R/R_{0,max}$ values remain low (1.5–2). This also results in an increased strain range where yielding progresses (marked in green), but the electrical resistance still does not deviate from theoretical values. For all three film systems, the stress plateau upon unloading is less pronounced compared to the brittle films discussed earlier.

Stress-strain curves recorded in the transverse direction have two noticeably different shapes, following the clear distinction between brittle and ductile film systems. The initial development of tensile stresses before fracture (grey curves in Figure 3) can be explained via a combination of Poisson's ratio mismatch and 2D shear lag,[38] as detailed in our previous publication.[15] Once cracks/necks begin to form, transverse stresses drop in all films (peak in grey curves, Figure 3), either through a relaxation mechanism or the build up of compressive stresses. Upon unloading, brittle Al films (0, 1, and 25 nm IL) experience an increase in transverse stress, while ductile Al films (0.14, 5, and 10 nm IL) experience a decrease in transverse stress. There is no evidence of buckling/local delamination in this strain regime (relaxation of transverse compressive stresses during loading[38]), confirmed by post-mortem SEM imaging. Upon unloading, all films eventually return to a quasi-neutral stress state.

2.3. Equi-biaxial tensile testing

Equi-biaxial loading conditions are particularly relevant for flexible electronics applications where devices experience multidirectional stresses during operation. Correlating X-ray diffraction, FWHM, and electrical resistance measurements enables the precise identification of failure mechanisms and provides quantitative metrics to compare system performance across different interlayer thicknesses.

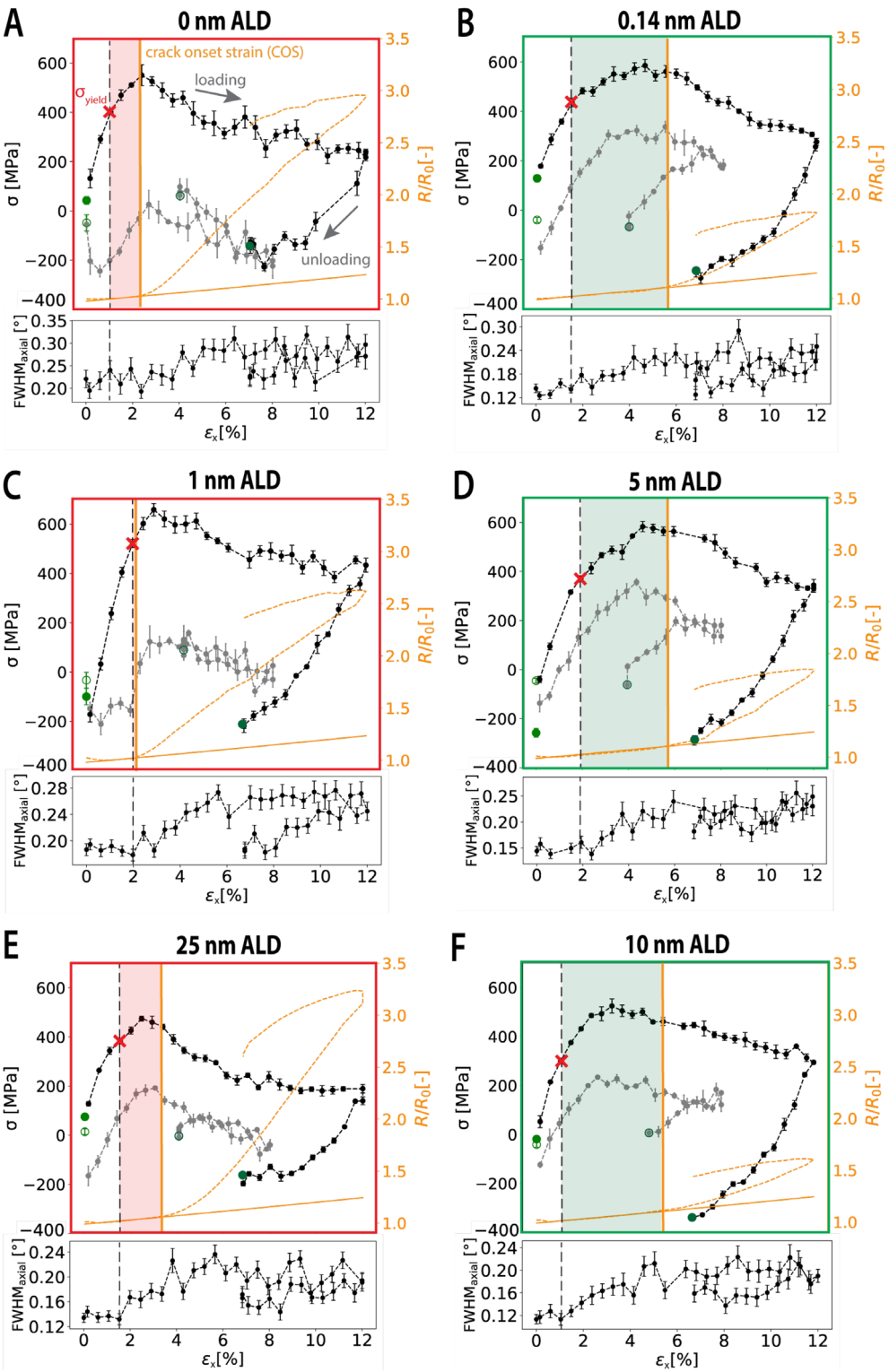

Figure 3. Al film stress, normalized electrical resistance (orange), and FWHM in axial direction as a function of applied strain (loading and unloading) measured from in situ uniaxial tensile experiments. A: Al/PI without ALD interlayer. B: 0.14 nm ALD interlayer. C: 1 nm ALD interlayer. D: 5 nm ALD interlayer. E: 25 nm ALD interlayer. F: 10 nm ALD interlayer. Yield stresses are marked with a red cross. Residual stresses measured at the start and end of each experiment are marked with a full (axial) or empty (transverse) green circle symbol. Note that in the transverse (grey) direction, films were only strained to 8%. The strain range from yield stress to damage onset is marked with red or green areas for brittle and ductile systems, respectively. Brittle cases are marked with a red frame, while ductile ones are marked with a green frame. Note that the 0 and 5 nm IL datasets (A and D) were reproduced from ref. [15].

Figure 4 summarizes the electro-mechanical deformation behaviour of the bilayers in equi-biaxial tension. The figure displays the changes in aluminum film stress (black curves), full width half maximum evolution (blue curves, FWHM at $\chi = 90°$ ($\hat{=}\ \psi\ 0°$), Al (111) peak) and measured and theoretical normalized electrical resistance (orange curves) during loading and unloading for each IL thickness ranging from 0 to 25 nm. As with the uniaxially tested samples, FWHM peak broadening correlates with higher defect concentrations and strain variations within the metal thin film,[42,43] providing insight into different deformation domains.[26] Additional FWHM data for all χ angles can be found in Figure S3 (Supporting Information). For all samples, a change in data acquisition density to decrease the measurement time resulted in a slight upward jump in FWHM values. Note that for the 0 nm IL sample, FWHM at $\chi = 80°$ was used due to better data quality. Correlation of the stress and FWHM evolution reveals four distinct deformation phases during loading:[30] an elastic region (I) characterized by linear stress-strain relationships and constant FWHM values; a micro-plastic region (II) marked by curvature in the stress-strain relationship and increasing FWHM as dislocations begin to form; a necking/localized plastic deformation region (III) exhibiting constant or slightly decreasing stress but FWHM increasing at a different rate; and finally, a fragmentation region (IV) where stress decreases at a higher rate, while FWHM remains constant. The normalized electrical resistance reveals crack onset strain and offers a third correlative dataset for region IV, even if it does not directly match domain boundaries. Although theoretically possible, the sensitivity of the electrical resistance measurements is too low to detect deformation related to region II and III. Compared to a stress plateau in domain (III), decreasing stress in this region correlates with earlier crack onset and leads to a rapid electrical resistance increase in (IV). Post-mortem images of biaxially strained samples will be discussed in the following section 2.4.

As with the uniaxially tested samples, the Al films with 0, 1 nm and 25 nm interlayer (Figure 4A,C,E) exhibit brittle deformation behavior, with stresses decreasing as soon as the maximum stress has been reached. The 0 nm IL sample has the lowest yield stress-COS difference (0.2%) of all samples, and the electrical resistance deviates to very high values almost immediately. For the 1 nm IL system, the beginning of necking in the Al film (domain III) coincides well with the deviation of R/R_0 from the theory line (COS). After the onset of fragmentation ≈4%, R/R_0 increases rapidly from 1.4 (25% deviation from theory line) to a final value of 3 due to through-thickness crack formation. With 25 nm IL, R/R_0 deviates at 3.5% strain, well within the necking regime (2%), but before fragmentation is detectable in film stress and FWHM curves (4%). Progressive through-thickness cracking induces a rapid increase in electrical resistance with an $R/R_{0,max}$ value of 2.2. FWHM curves are similar for the three films, with the 1 nm IL film attaining higher absolute FWHM values and the 25 nm IL film plateauing in region IV. Additionally, there is no increase in FWHM during unloading for the 0 nm IL film. As with the uniaxially tested samples, the strain range between yield and crack onset is reduced (1–2%) compared to the other sample group (0.14, 5, and 10 nm IL). Upon unloading, compressive stresses accumulate linearly in the Al layers but do not reach a plateau. Therefore, a compressive yield stress cannot be unambiguously identified. Best approximations based on a correlation of a change in the linearity in the stress-strain curves and a simultaneous increase in FWHM (for most samples) are marked in Figure 4 with blue crosses.

In contrast, Al films with 0.14, 5 and 10 nm thick ILs (Figure 4B,D,F) show a more ductile deformation behavior with a pronounced stress plateau (domain III) either immediately after reaching the yield stress (0.14 nm IL) or after a bending over of the stress-strain curve (5 and 10 nm IL). Deformation in the Al layer is detectable as an electrical resistance deviation toward the end of domain III, at higher applied strains (≈5%) compared to the brittle films. Fragmentation causes stress relaxation for the 0.14 and 5 nm IL films after the plateau, whereby a steeper drop causes higher $R/R_{0,max}$. As straining of the 10 nm IL film stopped at 5.5%, the film does not experience electrical resistance deviation within the tested strain range, and it is possible that fragmentation would occur at higher strain levels. However, the strain-stress curve until 5.5% strain and the uniaxial experiment attest to ductile deformation. In contrast to the brittle samples, the strain range between yield and crack onset is increased (3–4%), attesting to more ductile deformation behavior for these three samples. FWHM curves are similar, whereby the maximum values vary with IL thickness without any clear trend. It should be noted that the Al films with 0 and 10 nm IL have higher initial FWHM values compared to all other films, possibly because of larger variations in grain size. After unloading, all ductile films exhibit a compressive stress plateau. Compressive yield stresses (blue crosses in Figure 4) were determined in the same manner as for the brittle samples.

During unloading, all Al layers show incomplete FWHM recovery, with the 0 nm IL sample having the highest recovery value. FWHM recovery is defined as the percentage difference between the lowest FWHM unloading value and the starting value. The lowest recovery value (57%) is observed with 0.14 nm IL, in contrast to recovery values of 71–74% with 1, 5 and 25 nm IL thickness. It should be noted that the 0.14 nm IL film system also exhibits the highest absolute FWHM values at the end of loading. Only the 0 and 10 nm IL films show almost full FWHM recovery (87%), whereby the lower maximum strain value for the 10 nm system could influence FWHM recovery. The 0 nm IL system has a clearly distinct FWHM curve compared to all ALD interlayer systems, with no increase in FWHM during the unloading period.

2.4. Post-Mortem SEM

Film stress and electrical resistance evolution correlate with the crack pattern that develops in the Al film. Post-mortem scanning electron microscopy (SEM) images taken after straining are shown in **Figures 5** and **6** for different IL thicknesses. To enhance deformation effects and minimize crack closure due to relaxation of the polymer after unloading, representative examples strained to 40% are shown for the uniaxial case.

Al films with 0, 1, and 25 nm IL (Figure 5A,C,E) show brittle crack patterns perpendicular to the tensile direction. Buckling induced by transverse stresses only occurs at high applied strains ≈40%. The buckling behavior of these systems is not part of the presented study and will be investigated in a forthcoming work. The reference film without ALD has significantly longer

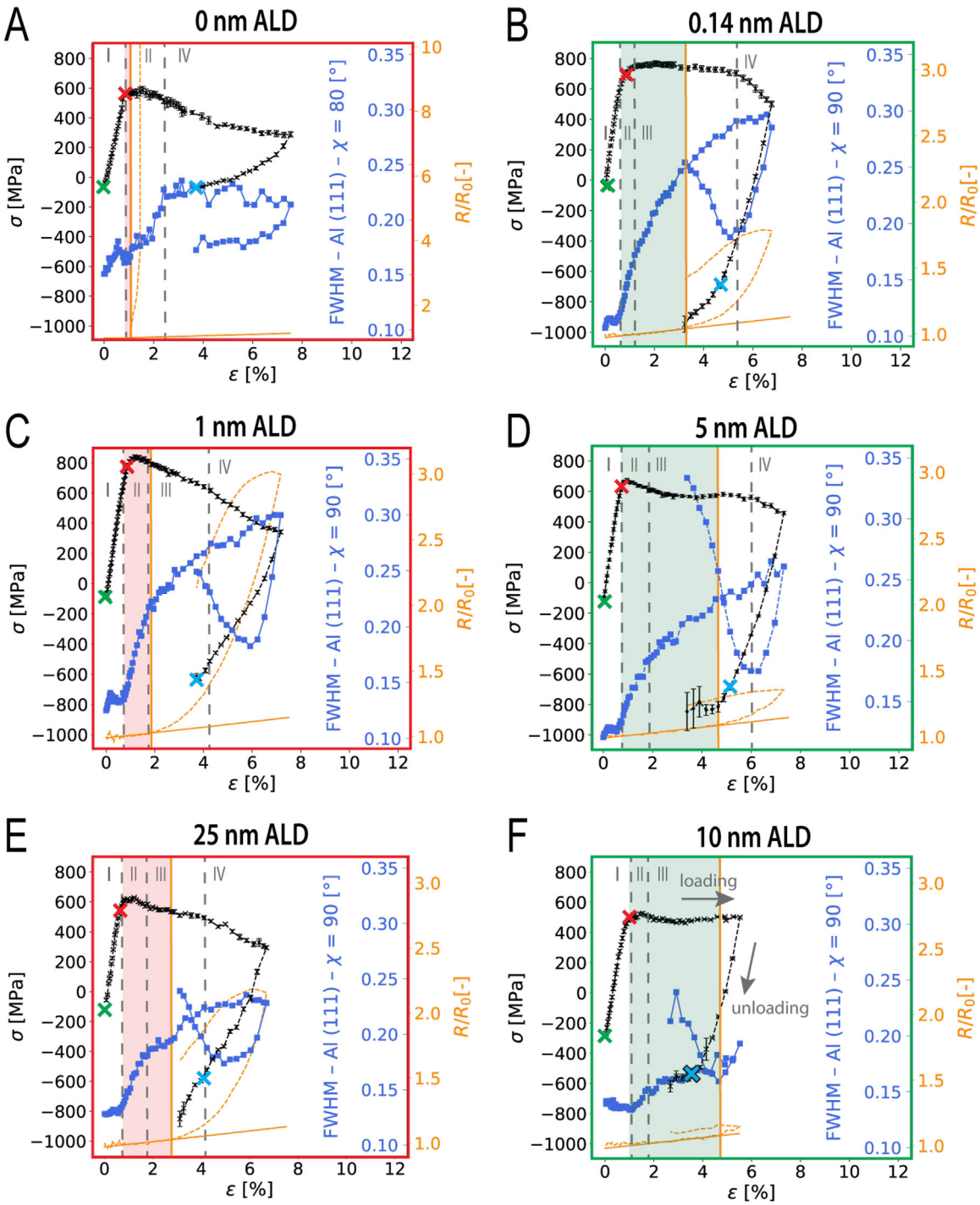

Figure 4. Al film stress (black), FWHM (Al (111) peak, blue), and in situ normalized electrical resistance (orange) as a function of applied strain (loading and unloading), measured from in situ XRD equi–biaxial tensile experiments. A: Al/PI without ALD interlayer. B: 0.14 nm ALD interlayer. C: 1 nm ALD interlayer. D: 5 nm ALD interlayer. E: 25 nm ALD interlayer. F: 10 nm ALD interlayer. Grey vertical lines illustrate different deformation domains during loading (I: elastic, II: micro–plastic, III: necking, IV: fragmentation). Measured residual and calculated 0.2% yield stresses during loading (tensile) and unloading (compressive) are marked with green, red, and blue crosses, respectively. The strain range from yield stress to damage onset is marked with red or green areas for brittle and ductile systems, respectively. Brittle systems are additionally marked with a red frame, while ductile systems are marked with a green frame. Note that in A, the R/R_0 scale is different and that in F, the 10 nm ALD interlayer sample was only strained to 5.5%. The 5 nm IL dataset (D) was adapted from.[15]

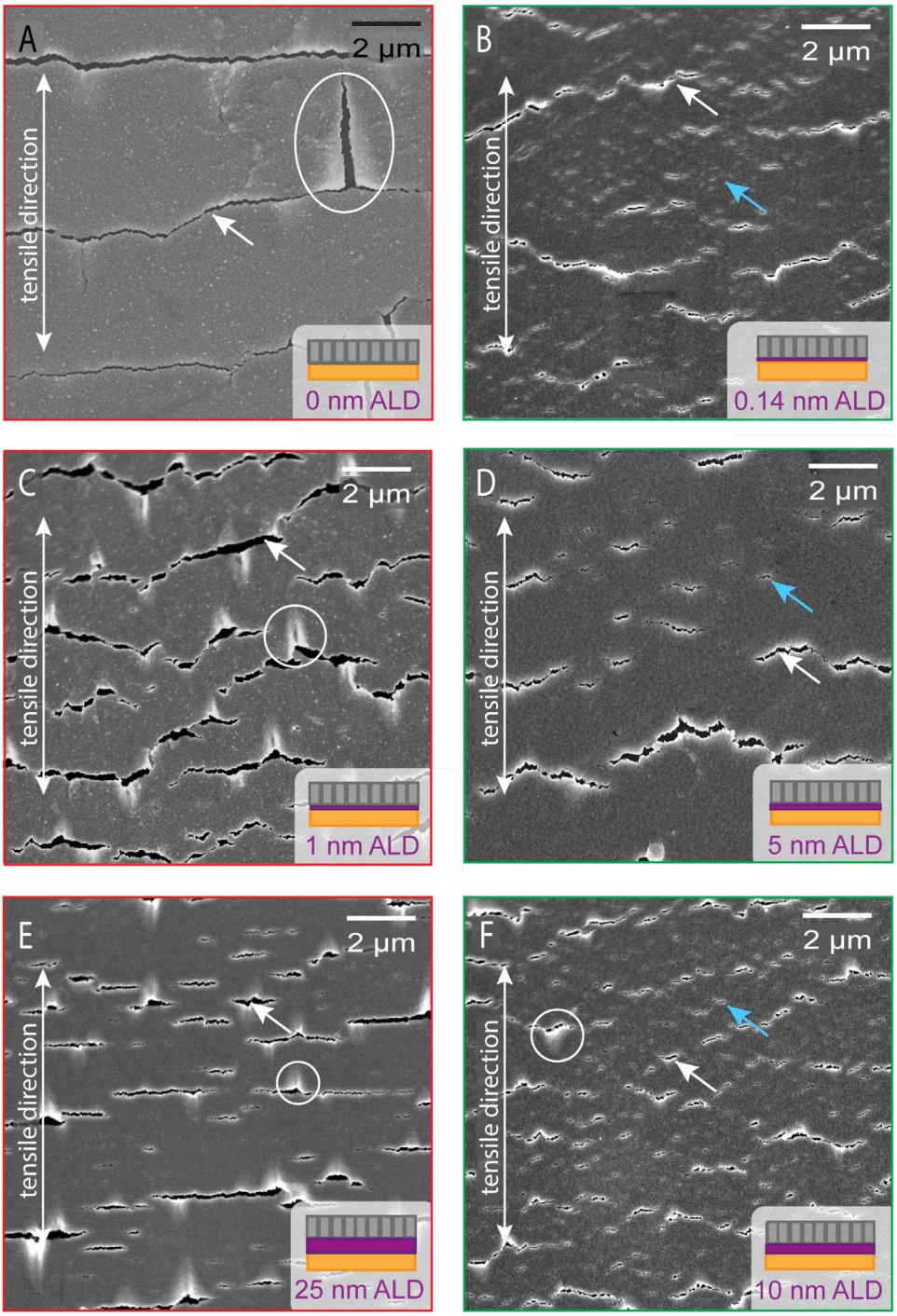

Figure 5. Post-mortem SEM images of Al thin films strained uniaxially to 40%. A: Al/PI without ALD interlayer. B: 0.14 nm ALD interlayer. C: 1 nm ALD interlayer. D: 5 nm ALD interlayer. E: 25 nm ALD interlayer. F: 10 nm ALD interlayer. Cracks are indicated with white arrows, while necking is indicated with blue arrows. The tensile direction is indicated with a double-headed white vertical arrow. Local delamination (buckles, marked with white circles) only form at strain level close to 40%, and are not considered in this work.

cracks than the other two systems, but a comparable saturation crack spacing λ_{sat} to 1 nm IL (distance between cracks, $\lambda_{sat,0nm}$ = 4.41 ± 1.42 μm, $\lambda_{sat,1nm}$ = 4.52 ± 1.29 μm). With 1 nm IL, the Al film exhibits angled cracks comparable to ductile systems, however, cracks are more open. Pronounced opening of cracks has been reported for Al films after extreme thermal cycling, accompanied by a higher normalized electrical resistance.[44] Between open cracks, there is little deformation and a significant amount of tensile-induced delamination (buckles, marked with white circles). With 25 nm IL thickness, the Al film exhibits the

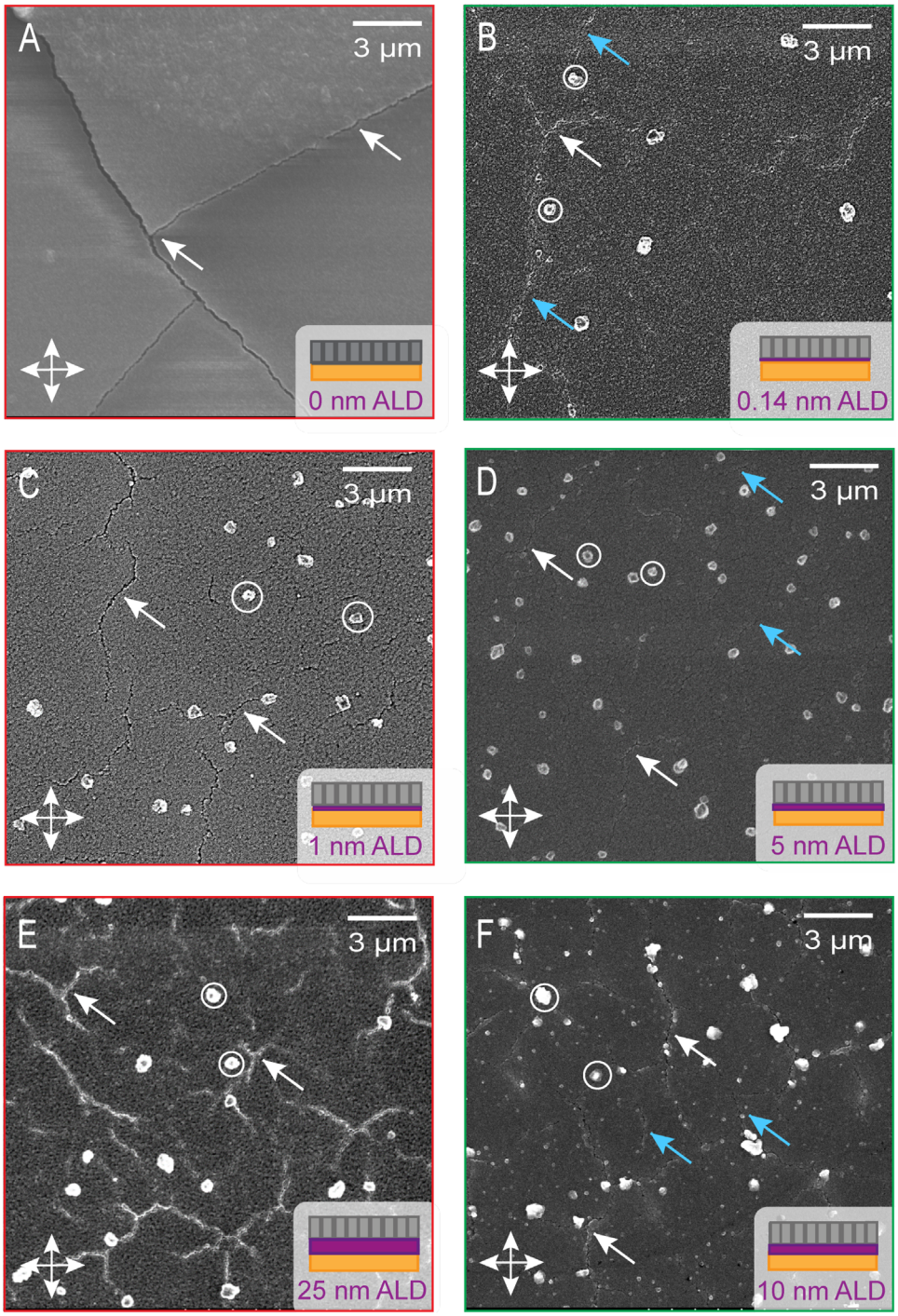

Figure 6. Post-mortem SEM images of equi-biaxially tested samples. A: Al/PI without ALD interlayer. B: 0.14 nm ALD interlayer. C: 1 nm ALD interlayer. D: 5 nm ALD interlayer. E: 25 nm ALD interlayer. F: 10 nm ALD interlayer. Cracks and necks are indicated with white and blue arrows, while hillocks grown during the deposition are indicated with white circles. Double-ended arrows indicate the tensile directions.

straightest cracks and a smaller crack spacing ($\lambda_{sat,25nm}$ = 3.69 ± 1.25 µm). In contrast, Al films with 0.14, 5, and 10 nm thick ILs (Figure 5B,D,F) show ductile cracking behavior with short, angled cracks, as well as necking / damage between cracks. In particular, the Al film with 0.14 nm IL exhibits the largest crack spacing in the ductile series ($\lambda_{sat,0.14nm}$ = 3.83 ± 0.69 µm).

Equi-biaxially tested samples exhibit typical mud-crack patterns,[26] shown in Figure 6. Cracks visible on the surface are indicated with white arrows, necking with blue arrows, and growth hillocks with white circles. Within the sample series, the reference Al film without ALD (Figure 6A) shows a distinctly different brittle cracking behavior, with sharp-edged fragments

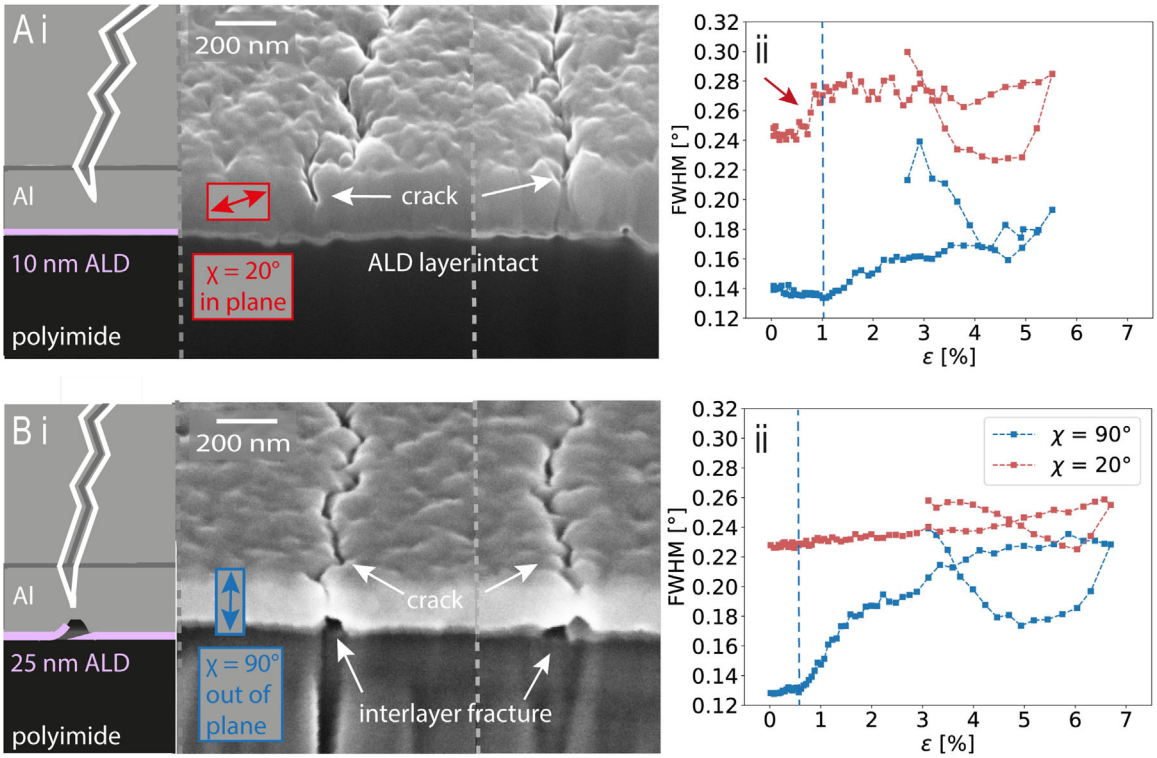

Figure 7. FIB/SEM cross-section images of cracks (i) and FWHM curves at $\chi = 90$ and 20° (ii) of thin film systems strained to 12%. A: 10 nm ALD interlayer system. B: 25 nm ALD interlayer system. Note that the FWHM curves were only recorded to 5.5 and 7%, respectively. The modes of damage initiation (through Al layer necking (A) or interlayer fracture (B)) are shown schematically next to the cross-sections. The white vertical stripes in B i are FIB damage to the substrate due to polishing the cross-section. For FWHM curves at $\chi = 90°$ (blue), the increase is marked with a blue dotted line (domain II), while the increase of the $\chi = 20°$ FWHM curve (A ii, red) is marked with a red arrow.

forming. All other samples show mud-crack patterning with smaller fragments, but cracks are sparse and very difficult to distinguish up to an IL thickness of 10 nm, due to the lower applied strain.

In the film thickness direction, FIB/SEM cross-sectioning of samples strained to 12% reveals crack origin and morphology, as seen in **Figure** 7A,B i. Representative cracks in the 10 and 25 nm IL systems are shown, to provide two contrasting datasets (ductile and brittle deformation) and to ensure that the IL can still be resolved. With 10 nm IL thickness, the crack propagates from the surface, initiated through necking of the Al film, while the interlayer remains intact. In contrast, with 25 nm IL thickness, fracture occurs at the interface, with a defect occuring at the ALD-substrate interface, facilitating damage of the Al film. These differences in crack morphology might play a role in the corresponding FWHM evolution recorded at $\chi = 90°$ and 20° (blue and red curves in Figure 7 ii, respectively). At $\chi = 20°$ ($\hat{=}\ \psi = 70°$), due to high sample tilt, in-plane changes in the thin film are predominantly measured.[45] Data recorded at $\chi = 90°$ represents the out-of-plane measurement direction. For the 10 nm IL system, FWHM increases in both angles (abruptly in $\chi = 20°$ at 0.7% strain), while with 25 nm IL, the $\chi = 20°$ curve stays constant throughout loading. The origin of this difference is subject of ongoing investigations.

3. Discussion

We can conclude from the uni- and biaxial test campaigns that varying the thickness of the ALD interlayer between the polyimide substrate and the Al thin film over two orders of magnitude does not yield a linear trend of mechanical response. Rather, it divides the series into three more brittle (0–1–25 nm) and three ductile (0.14–5–10 nm) thin film systems. This non-linear transition between brittle and ductile electro-mechanical behavior reflects fundamental changes in deformation mechanisms at the metal-oxide interface. Responsible competing mechanisms related to substrate functionalization, ALD-oxide layer consolidation, and thickness-dependent intrinsic ductility of ALD-oxides will be detailed in the following paragraphs.

3.1. Governing Mechanisms at Different ALD Interlayer Thicknesses

Independent of the loading condition, the reference Al film without ALD shows the most brittle behavior within the series (straight through-thickness cracks in Figures 5 and 6). The brittleness compared to literature originates from the specific interface and microstructure under the chosen deposition conditions.[21,46,47] This implies that chemical reactions

responsible for interfacial intermixing are compromised at RT and that additionally, the small Al grain size impairs ductility. For further details readers are referred to our recent publication.[15] Considering that one ALD cycle (0.14 nm IL) does not result in full surface coverage (process dependent, 40%[48] Al_2O_3 on PI), we attribute the observed Al ductility in this configuration to enhanced chemical intermixing at the interface rather than the IL itself. This means viewing the 0.14 nm interlayer as a surface activation mechanism, adding functional groups to the polymer surface[49] similar to plasma treatment. Surface activation facilitates intermixing reactions with subsequently deposited metal atoms;[49] the resulting native interlayer benefits adhesive and mechanical properties by promoting annihilation of dislocations at the interface.[46]

In our recent work, we compare the performance of a 5 nm ALD interlayer to a 5 nm intermixed interlayer and demonstrate how the added ductility of the Al film with 5 nm ALD compared to the brittle Al reference film is a direct result of the interface structure[15] (published in 2025). The ALD-interlayer's ability to enable dislocation activity and localized plastic deformation in Al does not extend to 1 nm thickness, the problem likely being incomplete coalescence of ALD. On polyimide substrates, uniform and dense growth of the ALD layer is predicted from ≈3 nm (20 cycles).[48] Below this thickness cut-off the ALD layer follows an island-growth mode.[50,51] Resulting ALD islands locally inhibit intermixing reactions and native interlayer formation between subsequently deposited Al atoms and the PI substrate, creating an inhomogeneous and mechanically weak interface. However, a continuous 1 nm ALD interlayer is expected to perform at least as well as its 5 nm counterpart based on observations in nanolaminates.[20,52] The transition from ALD islands to a coalescent layer is faster if the number of nucleation sites is higher, which could be achieved by preceding plasma treatment.[49,53]

When increasing the ALD-IL thickness from 5 to 10 nm, Al films remain ductile due to intrinsic IL ductility, evidenced by the intact IL in crack cross-sections (Figure 7A i) after 12% applied strain. In contrast, at 25 nm IL thickness, all analyses attest brittle deformation behavior to the Al films and the IL itself. These findings align with reports on ALD-oxides becoming intrinsically brittle and mechanically weak with increasing layer thickness, even though the critical thickness values vary. In Al/Al_2O_3 nanolaminates, comparable oxides are brittle already from a thickness of 9.4 nm in both uniaxial and equi-biaxial tension.[21,22] Similar behavior was found in micropillar compression, where oxide layers fractured with thicknesses above and including 5 nm.[20] In flexible thin film transistors, the electrical performance only degrades once the amorphous Al_2O_3 IL is thicker than 30 nm.[17] Compared to nanolaminates, the Al_2O_3 layer is closer to the PI substrate in the transistor design. This further underscores the critical role of layer order, as proximity to the polymer substrate is expected to enhance ductility.[30] At higher oxide thicknesses of 50 nm, Al_2O_3 films deposited directly onto a Polyimide substrate were found to fracture starting at 0.77% strain.[54] Additionally, at these oxide thicknesses, the ALD layer has a higher volume fraction in the total system, which is another contributing factor to brittle behavior.

3.2. Von Mises Biaxial Yield Surface and Strengthening Mechanisms

All Al films (brittle and ductile) showed a certain nonlinearity in the stress-strain curves before mechanical failure. Once unloaded, all systems finished in a higher compressive stress state, further proof of plastic deformation. Therefore, experimentally determined uniaxial and biaxial yield stresses were used to calculate the complete biaxial stress dependence of Al layer plasticity using the von Mises yield criterion (1913), similar to.[21,37] If a material breaks in the elastic domain (classic definition of brittle), the yield surface from Von Mises criteria is no longer valid.

The calculated von Mises ellipses are shown in **Figure 8A** for all IL thicknesses, also including the reference Al film without ALD interlayer. Uniaxial data points are marked with open symbols. Due to the Poisson's ratio difference between metal film and polymer substrate, nominally uniaxial experiments are by nature slightly biaxial. To determine the axial and transverse 0.2% yield stress components (marked with red crosses in Figure 3) for uniaxially strained samples, a deviation from the axial linear stress-strain response together with an increase in FWHM was considered. Equi-biaxial datapoints are marked with filled symbols. The higher density of acquired data points during equi-biaxial testing enables determination of 0.2% yield stresses from measured stress-strain curves via the strain offset method.

The shapes of all calculated ellipses support the validity of the von Mises theory for our sample series. The reference film (0 nm IL sample) is the least eccentric (most round), evidencing more brittle behavior comparable to Al films tested in ref. [21]. To quantify the ellipse shape, the aspect ratio a, defined as the ratio between minor and major axes of the ellipse, was calculated. Aspect ratio values range from $a_{0.14nm} = 0.19$ to $a_{0nm} = 0.54$. Notably, samples exhibiting brittle deformation behavior (0, 1 and 25 nm) have larger aspect ratios (= lower eccentricity) of 0.54, 0.45, and 0.30, respectively, which aligns well with previous research findings.[21] Furthermore, all Al films demonstrate greater strength in equi-biaxial loading conditions, consistent with the prediction that metallic thin films perform stronger under equi-biaxial testing (e.g. 50 nm Ni, aspect ratio 0.4).[26] The difference is most pronounced for Al films with 0.14 and 5 nm IL. With increasing oxide thickness, where oxide deformation or fracture progressively dominates Al yield,[21] Al in Al/Al_2O_3 nanolaminates previously demonstrated weaker performance only when subjected to biaxial tension (ALD-oxide thickness 0.14–9.4 nm). This resulted in a higher eccentricity and inversion of the corresponding ellipses, however, it is not the case for 10 and 25 nm IL samples in our study. Thus, even though a higher interlayer thickness leads to lower yield stresses (10 and 25 nm samples), it does not strongly influence one loading case in particular.

The unloading portion of the equi-biaxial straining experiment provided compressive yield stress values, marked as squares in Figure 8A. It is important to note that these films had already experienced tensile loading and were not in a pristine stress state. Nevertheless, most values correspond well with the von Mises ellipses calculated using loading values, except the 0 and 1 nm IL samples. Only the 0 nm IL sample deviates completely, likely due to extensive through-thickness cracking. Unloading stress values from the uniaxial experiment were excluded from our analysis

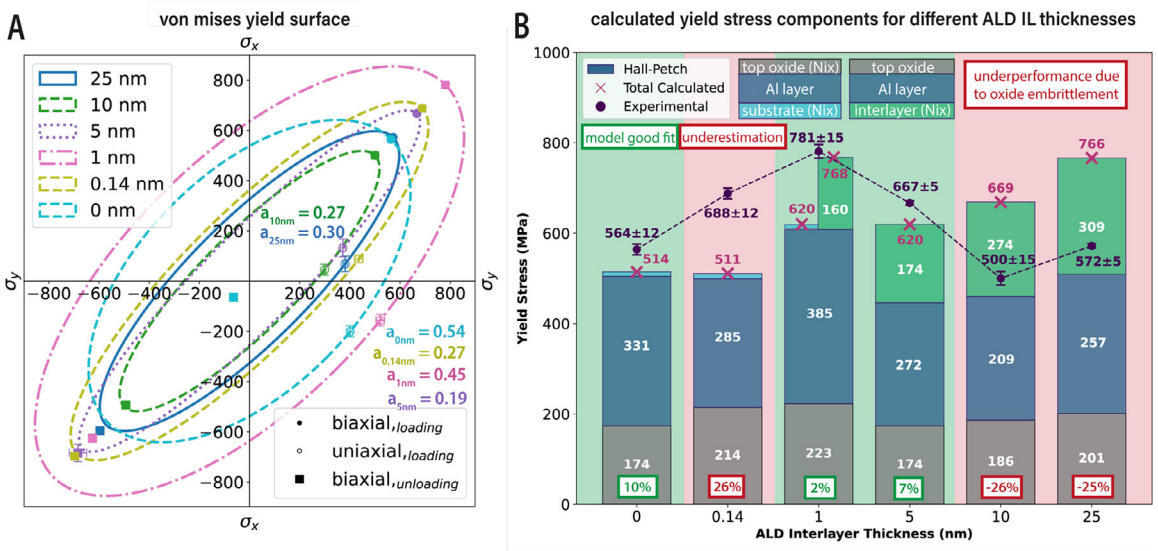

Figure 8. Von Mises yield surface and calculated yield stress components for different ALD IL systems. A: Biaxial stress dependence of plasticity of Al/IL/PI systems using the von Mises yield criterion. Data points obtained from uni- and equi-biaxial tensile testing are included on the right side using open and closed circle symbols, respectively. For comparison, equi-biaxial unloading yield stresses are included in the lower left quarter. Calculated aspect ratios, *a*, for all ellipses are displayed in the respective color. B: Calculated yield stress components for different IL thicknesses compared to experimental values. The Al layer-top oxide (Nix model) and Hall-Petch contributions were considered for all IL systems. For the 0, 0.14, and 1 nm cases a substrate-Al layer interaction was considered, while for the 1, 5, 10, and 25 nm IL cases an interlayer-Al layer interaction was taken into account.

due to the ambiguity in distinguishing between crack closure and film deformation effects. Uniaxially, films were tested to 12% strain, almost double the value of the equi-biaxial straining experiment (7% strain).

To account for the effect of layer thickness, grain size, and interface type on yield stress, our experimental data is compared to different thin film mechanics models. The Nix model combined with the Hall-Petch (H-P) relation[55,56] provided the best fit (Equation 1 and 2, pink crosses and multi-colored bar chart in Figure 8B). The Nix model considers the deposition of dislocation segments during dislocation glide at the top and bottom interfaces of the metal film[55] as the main contributor to thin film strength. In contrast to the Thompson and source models,[32] both the top and bottom interfaces are taken into account. To account for grain size, a Hall-Petch term (Equation 2) has been added to the calculated yield stress $\sigma_{yield,Nix}$. This approach allows for the separation of different contributions to the yield stress, namely the top native oxide-Al layer interaction (grey bars in Figure 8B), the Al grain size (Hall-Petch relation, blue bars in Figure 8B), and the polymer substrate or interlayer-Al layer interaction (light blue and green bars in Figure 8B). All of these components are influenced by the Al film thickness *h*. A comparison of the theoretical yield stresses calculated using different approaches (Nix+H-P, Thompson, and source models) with the experimental data can be found in the supporting information (Figure S4).

$$\sigma_{yield,Nix+H-P} = 3.464 \cdot \frac{b}{2\pi \cdot (1-\nu) \cdot h} \cdot \left[\frac{\mu_f \cdot \mu}{\mu_f + \mu} \cdot \ln\left(\frac{\beta \cdot t}{b}\right) + \frac{\mu_f \cdot \mu_o}{\mu_f + \mu_o} \cdot \ln\left(\frac{\beta_o \cdot t_{TO}}{b}\right) \right] + \sigma_{yield,H-P} \quad (1)$$

was used for yield stress calculations in Figure 8B, with the H-P contribution[56] described as:

$$\sigma_{yield,H-P} = \sigma_0 + K * d^{-\frac{1}{2}} \quad (2)$$

Variables are defined as $\sigma_0 = 11.3$ MPa (bulk strength of Al), $K = 0.07$ MPa $m^{\frac{1}{2}}$ (Hall-Petch constant),[57] $b = 0.286 * 10^{-9} m$ (Burgers vector), $\beta_o = 17.4$, $\beta_s = 2.6$ (constants), $\mu_f = 24.8\ GPa$, $\mu_o = 178.9\ GPa$, $\mu_s = 1\ GPa$ (shear moduli of film, oxide, and substrate), $\nu = 0.31$ (Poisson's number of Al), t (IL or Al layer thickness) and t_{TO} (native top oxide thickness). In Equation 1, the first term in square brackets describes the substrate or interlayer-film interaction, while the second term represents the film-top oxide interaction. For the 0, 0.14, and 1 nm IL systems a substrate-Al layer interaction was considered in the first term (substrate constants μ_s, β_s, and Al film thickness h for μ, β, and t, respectively). For the 1, 5, 10, and 25 nm IL systems, an oxide interlayer-Al layer interaction was considered (oxide interlayer constants μ_o, β_o, and IL thickness t_{IL} for μ, β, and t, respectively). Dependent on the Al layer thickness and measured grain size, an adapted correction factor ranging from 1 (infinitely thick layer) to $\frac{\pi}{2}$ (infinitely thin layer) was applied to the grain size before the calculation.[58] All calculated values are compared with those measured experimentally (violet points) in Figure 8B.

For the reference Al film without an ALD interlayer, the model fits the system performance (10% deviation from the experimental value). This is comparable to a previous study of magnetron-sputtered Al on polyimide, where the same model was used.[15] In contrast, the 0.14 nm IL system has a significantly higher yield stress than predicted. This is possibly due to enhanced chemical interactions between Al and PI forming an additional interlayer whose contribution is not taken into account by the

model, therefore underestimating the system strength. In both cases, the main contributions to theoretical strength are the Al microstructure and native top-oxide. For the 1 and 5 nm IL systems the model shows a good fit, when taking into account the alumina interlayer. Even though our 1 nm ALD deposition is likely not continuous, as previously discussed, the model captures the experimental strength increase well. This is comparable to similar passivated metal layer systems investigated in ref. [32], where the Nix model slightly underestimated the yield stress. For the 10 and 25 nm IL systems the experimentally measured values fall short of the calculated yield stress, which can be attributed to oxide embrittlement. Post-mortem cross-sections in Figure 7B support stress concentrations at oxide fracture sites as the origin of Al embrittlement, similar to what has been observed in the case of adhesion-promoting Cr interlayers.[11] The Al crack coincides with interlayer fracture, which in turn has been shown to facilitate necking and through-thickness cracking.[10]

FWHM recovery during unloading serves as an additional parameter to identify strengthening mechanisms. All tested Al films show limited FWHM recovery, which is indicative of dislocations being blocked by the interface.[22,26] Full recovery is associated with partial dislocation nucleation and absorption at grain boundaries for grain sizes or film thicknesses < 100 nm.[21,59] A reduced recovery percentage points toward the ALD interlayer promoting dislocation storage in the metal film. However, the 0.14 nm IL system also shows reduced FWHM recovery, possibly involving a yet-undisclosed mechanism. In contrast, dislocations have been shown to disappear in the native interface,[46] while the native Al oxide on top acts as a dislocation barrier.[54] Amorphous oxides deform through strain localization in defects[60] or formation of shear bands, rather than confined layer slip (blocking of dislocations at the interface, model used above), which is only valid for crystalline nanoscale layers.[61] However, at such low oxide thicknesses, it is possible that the local volume is too small to accumulate enough energy for shear band formation, and this deformation mechanism is suppressed.[20,62] Consequently, if shearing of the interface is not possible, grain sliding or rotation is not easily accommodated, resulting in a strengthening effect of the interface. At higher oxide thicknesses, sufficient energy can be accumulated, and shear is possible, subsequently weakening the interface.

3.3. Correlation Between Mechanical and Electrical Failure

Regardless of the origin of plasticity, all ductile systems (0.14, 5, and 10 nm IL) show a large difference Δ in the applied strain value between Al yielding measured by XRD and damage/crack onset based on deviation of the electrical resistance from the theory (COS). The increased necking and short cracks for these systems (Figure 5) are numerous enough to affect the X-ray measurements but leave enough paths for electrons to percolate, not affecting electrical resistance measurements and delay electronic failure. This is an indication that a certain critical crack density (rather than a single crack as in brittle films[63]), triggers electronic failure. For brittle samples (0, 1, and 25 nm IL), the delta between applied strain at yield and COS is (sometimes negligibly) small. The 25 nm IL system consistently exhibits the largest delta within the brittle series. Therefore, the crack pattern developing from stress concentration at oxide fracture sites can be considered (electrically) more damage tolerant compared to an inhomogeneous interface. For biaxial straining, COS occurs consistently before domain IV (fragmentation) is identified in film stress and FWHM curves. This indicates that for 2D structural defects (mud-cracks) electrical resistance measurements are a more sensitive indicator for cracking than XRD. Generally, residual compressive stress levels in a thin film also shift crack onset to higher applied strains. For 50–100 nm-thick ALD-AlO_xH_y films on fused silica, tensile residual stresses have been reported.[64] The measured evolution of residual stress in the Al layers as a function of IL thickness (see Figure 4) mirrors the thickness-dependent stress evolution reported for ALD-Alumina on PI,[65] whereby higher tensile stresses in Al_2O_3 induce compressive stress in Al.

Crack morphology in the Al film changes distinctly in the presence of the ALD interlayer. Structural modifications at the interface have also been found to alter crack propagation behavior in other cases.[66] When strain localization occurs at the interface, it promotes straight through-thickness crack formation[8] and brittle failure. In contrast, well-bonded films exhibit enhanced strain accommodation and subsequently develop zigzag crack patterns.[67] Average crack lengths, difficult to determine from post-mortem SEM images, were calculated using the quantitative FEM-based model described in ref. [68]. The model uses $R/R_{0,max}$ and the saturation crack spacing λ_{sat} (through-thickness cracks only) for each sample. As crack density saturates after a certain point, the increase in normalized electrical resistance can solely be ascribed to an increase in crack length.[69] To account for a wide range in crack spacings, a range of crack lengths was calculated using standard deviations of the measured saturation crack spacing λ_{sat}. Calculated crack lengths corroborate post-mortem SEM images shown in Figure 5, with shorter cracks for ductile IL systems ($l_{0,0.14nm}$ = 2.0–5.1 µm, $l_{0,5nm}$ = 1.7–5.8 µm, $l_{0,10nm}$= 1.5–3.3 µm), and longer cracks for brittle systems ($l_{0,0nm}$ = 28.1–54.9 µm, $l_{0,1nm}$ = 8.7–15.6 µm, $l_{0,25nm}$ = 4.9–10.0 µm).

Although crack spacing alone cannot unambiguously determine ductility due to its statistical variability, crack length—derived from saturation crack spacing and the $R/R_{0,max}$ ratio—serves as a reliable ductility indicator. Shorter cracks dissipate energy through a plastic deformation component, which is crucial for ductile deformation. In situ XRD tensile testing data with electrical resistance measurements can be quantified by calculating the above mentioned strain difference Δ between COS and yield strain (green and red areas in Figures 3 and 4), providing a meaningful ductility metric. Systems with $\Delta >$ 2.5 exhibit ductile deformation characteristics, with a more pronounced difference between ductile and brittle systems for uniaxially tested samples. This criterion may serve as a practical design parameter for assessing the mechanical behavior of novel thin film systems. A graph that summarizes crack length, spacing, and Δ is shown as Figure S5 (Supporting Information).

Finally, in **Figure 9**, the behavior of our films is compared to multi- and bilayer systems with ductile and brittle components previously reported in the literature.[9–12,21,30,31,70] The deformation map shows possible layer combinations (with modulation

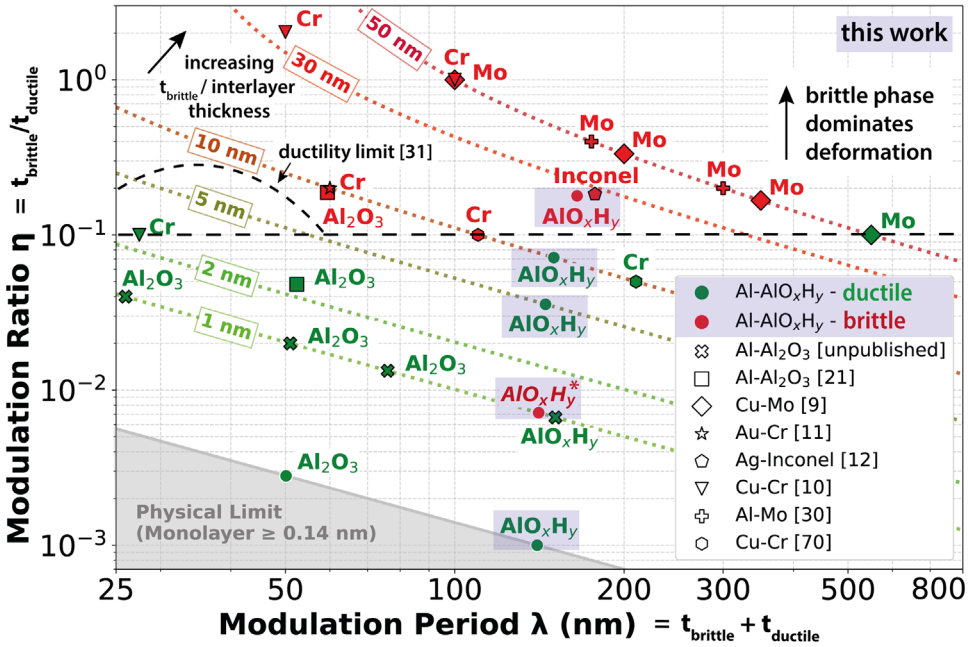

Figure 9. Length-scale-dependent deformation of thin films with brittle and ductile components. For our data, $t_{ductile}$ denotes the Al film thickness, while $t_{brittle}$ refers to the AlO_xH_y IL thickness. The grey region corresponds to a physically inaccessible region due to the ALD monolayer limit of 0.14 nm. Trend lines indicate the thickness of the brittle interlayer. Ductile samples are marked in green, while brittle samples are marked with red symbols. Our datapoints are marked with light blue highlighting and round symbols, while literature datapoints are bordered in black and marked with symbols detailed in the legend. From a modulation ratio of 0.1 or lower, ductile deformation behavior dominates. The asterix on the 1 nm AlO_xH_y IL sample denotes brittle deformation behavior due to incomplete ALD layer formation for this interlayer thickness. Note that nanolaminate samples with a fully formed 1 nm ALD layer are ductile for similar Al layer thicknesses (green crosses).

period $\lambda = t_{brittle} + t_{ductile}$ and modulation ratio $\eta = \frac{t_{brittle}}{t_{ductile}}$, where t is equal to the film thickness) and dashed guidelines that correspond to the respective brittle layer thickness. For samples in this work, $t_{ductile}$ refers to the thickness of the Al layer, while $t_{brittle}$ denotes the AlO_xH_y IL thickness (even though ductile at low thicknesses). The physically inaccessible region in grey is drawn based on the ALD thickness limit of one monolayer (0.14 nm for Al_2O_3). Generally, data points become more sparse at lower modulation ratios, due to fabrication-dependent minimum thickness required for continuous films. Our samples (highlighted in blue) fit well into the predicted literature trend of preserved ductility (green data points) at the modulation ratio $\eta \leq 0.1$. The exception to this trend is the 1 nm IL sample, which shows brittle deformation behavior due to incomplete ALD layer consolidation yielding an inhomogeneous interface. However, samples in which the 1 nm IL formed fully (Al/ALD-Al_2O_3 nanolaminate systems, green crosses in Figure 9, data unpublished) show ductile deformation behavior. The modulation ratio η represents a valuable design parameter for flexible thin film systems in electronics and space applications, where values below 0.1 indicate expected ductile deformation behavior.

4. Conclusion

Uni- and equi-biaxial tensile straining with in situ XRD and electrical resistance measurements was carried out on sputter-deposited Al films on polyimide with amorphous atomic-layer-deposited (ALD) AlO_xH_y interlayers (IL) of varying thicknesses (0–25 nm). ALD interface engineering significantly improves the deformation behavior of the Al thin film. It is demonstrated that increasing IL thickness over two orders of magnitude does not yield a linear response in mechanical behavior. Instead, the complex interplay of interface homogeneity and oxide layer deformation divides the sample series into three ductile (0.14–5–10 nm) and three brittle (0–1–25 nm) cases. ALD can be used to enhance native intermixing (0.14 nm IL) or replace the native interlayer (5 and 10 nm IL), which facilitates Al ductility. Embrittlement at low (1 nm) and high (25 nm) IL thicknesses has different origins: below 3 nm, ALD island-growth on polymers yields an inhomogeneous interface with stress concentrators. Above 10 nm thicknesses, the ductile-to-brittle transition inherent to the oxide IL controls the system behavior through fracture, causing stress concentration and Al through-thickness cracking. The margin between mechanical and electrical failure criteria (σ_y and COS) is proposed as a quantitative measure of ductility. Our bilayers fit well within literature in a length-scale-dependent deformation map, and the modulation ratio η ($= t_{IL}/t_{ductile}$) is presented as a design parameter for flexible thin film systems. In flexible applications, from electronics to the space industry, additional constraints on individual layer thickness may arise from device functionality (e.g., surface protection, diffusion barriers, or electrical insulation). Therefore, understanding these competing mechanisms is all the more crucial for establishing design principles that enable device conformability over large strain ranges. Beyond immediate applications in flexible electronics and space technologies, our findings provide fundamental insights into how competing deformation mechanisms at heterointerfaces can

be leveraged to create materials with programmable mechanical and electrical responses.

5. Experimental Section

Synthesis of Bilayer Systems: Aluminum thin films (approx. 150 nm thick) were deposited on polyimide substrates (50 µm thickness, DuPont Kapton HN) via physical vapor deposition (PVD, magnetron sputtering), with and without amorphous (am)-AlO_xH_y interlayers. The interlayers were deposited via room temperature (RT)-ALD using the following pulse-exposure-purge precursor sequence: $Al(CH_3)_3$ (TMA, Dockweiler Chemicals GmbH), 0.2–0.5–20 s and H_2O, 0.15–1–20 s for 1, 6, 36, 70, and 179 cycles; nominal thicknesses 0.14, 1, 5, 10, and 25 nm. The deposition resulted in an am-AlO_xH_y layer with a measured growth per cycle (GPC) of 0.14 nm, consistent with RT alumina ALD processes.[71] The polymer substrates were pre-cut into testing geometries (tensile strips of 5 × 0.6 cm and cruciforms with an arm width of 20 mm see[72]) to eliminate the need for post-deposition processing that might affect edge integrity. All substrates underwent ultrasonic cleaning in sequential acetone and isopropanol baths (5 min each) prior to deposition. The deposition setup consisted of a hybrid ALD-PVD system (SwissCluster SC-1,[15,52] similar in design to[73]), using two planar high-purity Al targets (diameter 50.8 mm, purity 99.999%, HMW Hauner GmbH) positioned equidistant from the non-rotating substrate. The aluminum layer sputtering parameters (summarized in Table S1 in the supporting information) include a current of 280 mA, a base pressure lower than 2.2×10^{-6} mbar, a working pressure of $7–10 \times 10^{-3}$ mbar and a combined deposition rate between 0.075–0.157 nm s^{-1}. For the cruciform substrates, a mask was used to deposit 1 cm × 1 cm thin film squares in the center of each cruciform.

Microstructural and Chemical Characterization: TEM analysis (FEI Titan Themis 200 G3 probe-corrected, Thermo Fisher) operated at 200 kV was performed to determine aluminum grain size and Al/IL thicknesses after FIB cross-sectioning and lift-out (Tescan Lyra/XMU Dual Beam FIB: 240 pA for rough cutting, 45 pA and lower for polishing). Grain measurements used the line intersect method with a correction factor $\frac{\pi}{2}$ to account for FIB slicing effects.[58] Orientation mapping was performed in the same TEM using a NanoMEGAS ASTAR system for scanning precession electron diffraction (SPED) with a precession angle of 0.6° and a step size of 2 nm.

Electromechanical Testing: Mechanical testing included uniaxial and equi-biaxial tensile experiments with in situ X-ray diffraction (XRD) and electrical resistivity measurements at synchrotron radiation facilities BESSY II (KMC-2 beamline[74]) and SOLEIL (Diffabs beamline[75]), respectively. XRD (Al (111) Bragg reflection; KMC-2: wavelength 0.128 nm, spot size 250 µm, Bruker VÅNTEC 2000 detector, 5 ψ angles 0°–45°;[74] Diffabs: wave length 0.128 nm, spot size 300 µm, XPAD-S140 detector, $sin^2\psi$ analysis: 8 ψ angles 0°–70°) measured Al lattice strain. During uniaxial straining, axial and transversal Al lattice strains were measured, parallel and perpendicular to the tensile direction on two separate samples, respectively. The data evaluation routine for uniaxial measurements is available at.[76] Data processing used a custom Python 3 routine with pseudo-Voigt and Pearson VII function fitting. For the uniaxial measurements, a weighted linear regression was used for peak fitting, therefore focusing on the fits with higher quality. The error bars for each stress measurement result from a Gaussian propagation of uncertainty from the fitting error of the $sin^2\psi$ slope. For the biaxial measurements, the fitting error of the $sin^2\psi$ slope was used for the error bars. Lattice stress was calculated using X-ray elastic constants (XECs, 1.8436 x 10^{-5} Pa for untextured Al (111) reflections,[77] calculated from single-crystal elastic constants via the Hill model and the software ElastiX[78]). No XRD signal was obtained from the ALD interlayers due to their low thickness and amorphous nature.

Uniaxial tests utilized an Anton Paar TS600 device (maximum strain $\epsilon_{x,max}$ = 12% (axial) or $\epsilon_{x,max}$ = 8% (transverse), strain rate 4×10^{-5} s^{-1}) with integrated electrical resistance probes (only utilized in the axial measurement). The equi-biaxial experiment (preload 3 N, maximum strain ϵ_{max} = 8%, strain rate $3–9 \times 10^{-6}$ s^{-1} (increased in three stages for each experiment)) incorporated a 4-point-probe Van der Pauw resistivity setup.[79] Digital Image Correlation (DIC, on the backside of the samples)[26] correlated macroscopic (ϵ) to lattice strains.

Post-mortem SEM imaging (Hitachi S-4800, Japan, 10 kV) was used to image samples post-mortem to obtain crack density and spacing for both uni- and equi-biaxial samples. FIB cross-sections of samples strained to 12% were imaged to visualize the interlayer and the origin of cracks (TFS Magellan 400, 7 kV).

Statistical Analysis: For measurements of Al layer thickness and grain size, 30 measurements were taken from one TEM lamella for each condition and are given as mean ± SD in Table S2 (Supporting Information). Both uni- and biaxial stresses and associated full width half maxima (FWHM) are presented as mean ± SD in Figures 3 and 4, the residual and yield stresses are also given as mean ± SD in Table S3 (Supporting Information). The calculated errors for FWHM and film stress stem from the fitting error of the pseudo-Voigt and Pearson VII function to the diffraction peak and the $sin^2\psi$ linear fit, respectively. For both uni- and biaxial measurements, X error lies within the plotted data points. Errors for the resistance measurements are within 0.003 of R/R_0 (measurement accuracy according to the datasheet). For crack saturation spacing analysis, presented in the manuscript in Section 2.4, 40 crack spacings were measured for each condition from at least 3 different sample regions. To account for the statistical variance of crack saturation spacing, the mean value + and – SD was used to calculate crack lengths, which are given as ranges in Section 3.3 of the manuscript.

Supporting Information

Supporting Information is available from the Wiley Online Library or from the author.

Acknowledgements

The authors thank D. Gutnik (Department of Materials Science, University of Leoben) for help during the 2023 SOLEIL synchrotron beamtimes and Z. Ma (Nanometallurgy, ETH Zurich) for SEM imaging (Figure 6). The authors thank R. Spolenak (Nanometallurgy, ETH Zurich) for general discussion and P. Gruber (IAM-ZM, Karlsruhe Institute of Technology) for discussion on models for yield strength. The authors thank HZB for the allocation of synchrotron radiation beamtime and thank Daniel Toebbens for assistance in using the beamline KMC-II under proposal 231-11757-ST. The authors acknowledge SOLEIL for provision of synchrotron radiation facilities and thank Cristian Mocuta and Dominique Thiaudière for assistance in using the beamline DiffAbs under proposals 20220220, 20230260, and 20230080. P.O.R. acknowledges funding from ANR-18-EURE-0010. J.B. and B.P. acknowledge funding from the Swiss National Science Foundation under the Ambizione grant agreement No. PZ00P2_202089. B.P and D.F. acknowledge financial support from Université Sorbonne Paris Nord through its Invited Professor call (2024). C.O.W.T. acknowledges the financial support under the scope of the UFO program (SPM-PN 3022) by the Austrian State of Styria (Land Steiermark - Abteilung 12 Wirtschaft, Tourismus, Wissenschaft und Forschung). T.E.J.E. acknowledges funding from the European Union's Horizon 2020 research and innovation programme under the Marie Skłodowska-Curie grant agreement No. 840222 and the JSPS KAKENHI Start-Up grant (24K23036).

Open access publishing facilitated by ETH-Bereich Forschungsanstalten, as part of the Wiley - ETH-Bereich Forschungsanstalten agreement via the Consortium Of Swiss Academic Libraries.

Conflict of Interest

The authors declare no conflict of interest.

Author Contributions

J.B. contributed to conceptualization, investigation, visualization, writing – original draft preparation, and writing – review & editing. V.D., D.C.,

T.E.J.E., and S.A.H. contributed to investigation and writing – review & editing. C.O.W.T. and P.-O.R. contributed to investigation, methodology, software, validation, and writing – review & editing. D.F. contributed to investigation, methodology, validation, and writing – review & editing. M.J.C. contributed to investigation, funding acquisition, methodology, and writing – review & editing. B.P. contributed to conceptualization, funding acquisition, project administration, supervision, and writing – review & editing.

Data Availability Statement

The data that support the findings of this study are available from the corresponding author, B. P., upon reasonable request. Uniaxial synchrotron data are openly available in Zenodo at, https://doi.org/10.5281/zenodo.17581203 and the codes at, https://doi.org/10.5281/zenodo.17349575,[80].

Keywords

atomic layer deposition, electromechanical properties, flexible polymer substrates, tensile testing, thin films

Received: October 2, 2025
Revised: November 13, 2025
Published online:

[1] D.-J. Liaw, K.-L. Wang, Y.-C. Huang, K.-R. Lee, J. Lai, C. Ha, *Prog. Polym. Sci.* **2012**, *37*, 907.
[2] J. Moery, *Space Telescopes and Instrumentation I: Optical, Infrared, and Millimeter* **2006**, *6265*, 62653B.
[3] N. Montinaro, U. L. Cicero, F. D'Anca, E. Bozzo, S. Paltani, M. Barbera, *J. Astron. Telesc. Instrum. Syst.* **2023**, *9*, 034005.
[4] R. Haight, *Surf. Sci. Rep.* **1995**, *21*, 275.
[5] L. W. McKeen, *Film Properties of Plastics and Elastomers*, Elsevier, Amsterdam **2017**, 147.
[6] F. M. Mwema, O. P. Oladijo, S. A. Akinlabi, E. T. Akinlabi, *J. Alloys Compd.* **2018**, *747*, 306.
[7] L. J. Matienzo, F. D. Egitto, *Polym. Degrad. Stab.* **1992**, *35*, 181.
[8] N. Lu, X. Wang, Z. Suo, J. Vlassak, *Appl. Phys. Lett.* **2007**, *91*, 221909.
[9] M. J. Cordill, T. Jörg, D. M. Toebbens, C. Mitterer, *Scr. Mater.* **2021**, *202*, 113994.
[10] V. M. Marx, F. Toth, A. Wiesinger, J. Berger, C. Kirchlechner, M. J. Cordill, F. D. Fischer, F. G. Rammerstorfer, G. Dehm, *Acta Mater.* **2015**, *89*, 278.
[11] B. Putz, R. L. Schoeppner, O. Glushko, D. F. Bahr, M. J. Cordill, *Scr. Mater.* **2015**, *102*, 23.
[12] B. Putz, C. May-Miller, V. Matl, B. Voelker, D. M. Toebbens, C. Semprimoschnig, M. J. Cordill, *Scr. Mater.* **2018**, *145*, 5.
[13] D. D. Gebhart, A. Krapf, B. Merle, C. Gammer, M. J. Cordill, *J. Vac. Sci. Technol., A* **2023**, *41*, 023408.
[14] D. D. Gebhart, A. Krapf, L. Schretter, A. Lassnig, B. Merle, M. J. Cordill, C. Gammer, *Adv. Eng. Mater.* **2024**, *26*, 2400251.
[15] J. Byloff, C. O. W. Trost, V. Devulapalli, S. Altaf Husain, D. Faurie, P.-O. Renault, T. E. J. Edwards, M. J. Cordill, D. Casari, B. Putz, *ACS Appl. Mater. Interfaces* **2025**, *17*, 41224.
[16] L. Atanasoska, S. G. Anderson, H. M. Meyer, Z. Lin, J. H. Weaver, *J. Vac. Sci. Technol., A: Vacuum, Surfaces, and Films* **1987**, *5*, 3325.
[17] B. U. Hwang, D.-I. Kim, S. W. Cho, M. G. Yun, H. jun Kim, Y. J. Kim, H. K. Cho, N. Lee, *Org. Electron.* **2014**, *15*, 1458.
[18] W. Zuo, H. Chen, Z. Yu, Y. Fu, X. Ai, Y. Cheng, M. Jiang, S. Wan, Z. Fu, R. Liu, G. Cheng, R. Xu, L. Wang, F. Xu, Q. Zhang, D. Makarov, W. Jiang, *Nat. Mater.* **2025**, *24*, 735.
[19] E. J. Frankberg, J. Kalikka, F. G. Ferré, L. Joly-Pottuz, T. Salminen, J. Hintikka, M. Hokka, S. Koneti, T. Douillard, B. L. Saint, P. Kreiml, M. J. Cordill, T. Epicier, D. D. Stauffer, M. Vanazzi, L. Roiban, J. Akola, F. D. Fonzo, E. Levänen, K. Masenelli-Varlot, *Science* **2019**, *366*, 864.
[20] T. E. J. Edwards, T. Xie, N. M. della Ventura, D. Casari, C. Guerra, E. Huszár, X. Maeder, J. J. Schwiedrzik, I. Utke, L. Pethö, J. Michler, *Acta Mater.* **2022**, *240*, 118345.
[21] B. Putz, T. E. Edwards, E. Huszar, L. Pethö, P. Kreiml, M. J. Cordill, D. Thiaudiere, S. Chiroli, F. Zighem, D. Faurie, P. O. Renault, J. Michler, *Mater. Des.* **2023**, *232*, 112081.
[22] B. Putz, T. E. Edwards, E. Huszar, P. A. Gruber, K.-P. Gradwohl, P. Kreiml, D. M. Többens, J. Michler, *Adv. Eng. Mater.* **2022**, *25*, 2200951.
[23] S. V. Petegem, A. Guitton, M. Dupraz, A. Bollhalder, K. Sofinowski, M. V. Upadhyay, H. V. Swygenhoven, *Exp. Mech.* **2017**, *57*, 569.
[24] W. Yang, G. Ayoub, I. Salehinia, B. Mansoor, H. M. Zbib, *Acta Mater.* **2017**, *135*, 348.
[25] D. M. Collins, T. Erinosho, F. P. Dunne, R. I. Todd, T. Connolley, M. Mostafavi, H. Kupfer, A. J. Wilkinson, *Acta Mater.* **2017**, *124*, 290.
[26] D. Faurie, F. Zighem, P. Godard, G. Parry, T. Sadat, D. Thiaudiere, P. O. Renault, *Acta Mater.* **2019**, *165*, 177.
[27] M. N. Giovan, G. Sines, *J. Am. Ceram. Soc.* **1979**, *62*, 510.
[28] J. Andersons, Y. Leterrier, *Probab. Eng. Mech.* **2007**, *22*, 285.
[29] Y. Leterrier, D. Pellaton, D.-A. Mendels, R. Glauser, J. Andersons, J. E. Månson, *J. Mater. Sci.* **2001**, *36*, 2213.
[30] M. J. Cordill, P. Kreiml, B. Putz, C. Mitterer, D. Thiaudiere, C. Mocuta, P. O. Renault, D. Faurie, *Scr. Mater.* **2021**, *194*, 113656.
[31] K. Wu, J. Y. Zhang, J. Li, Y. Q. Wang, G. Liu, J. Sun, *Acta Mater.* **2015**, *100*, 344.
[32] P. A. Gruber, J. Böhm, F. Onuseit, A. Wanner, R. Spolenak, E. Arzt, *Acta Mater.* **2008**, *56*, 2318.
[33] G. Geandier, D. Thiaudiere, R. N. Randriamazaoro, R. Chiron, S. Djaziri, B. Lamongie, Y. Diot, E. L. Bourhis, P. O. Renault, P. Goudeau, A. Bouaffad, O. Castelnau, D. Faurie, F. Hild, *Rev. Sci. Instrum* **2010**, *81*, 103903.
[34] D. Faurie, O. Castelnau, R. Brenner, P. O. Renault, E. L. Bourhis, P. Goudeau, *J. Appl. Crystallogr.* **2009**, *42*, 1073.
[35] S. A. Husain, P. Kreiml, P.-O. Renault, C. Mitterer, M. J. Cordill, D. Faurie, *J. Vac. Sci. Technol., A* **2023**, *41*, 033403.
[36] M. Cordill, P. Kreiml, B. Putz, C. Trost, A. Lassnig, C. Mitterer, D. Faurie, P.-O. Renault, *Mater. Today Commun.* **2022**, *31*, 103455.
[37] S. Djaziri, D. Faurie, P. O. Renault, E. L. Bourhis, P. Goudeau, G. Geandier, D. Thiaudiére, *Acta Mater.* **2013**, *61*, 5067.
[38] S. Frank, U. A. Handge, S. Olliges, R. Spolenak, *Acta Mater.* **2009**, *57*, 1442.
[39] V. M. Marx, C. Kirchlechner, I. Zizak, M. J. Cordill, G. Dehm, *Philos. Mag.* **2015**, *95*, 1982.
[40] O. Glushko, M. J. Cordill, *Exp. Tech.* **2014**, *40*, 303.
[41] S. Frank, P. A. Gruber, U. A. Handge, R. Spolenak, *Acta Mater.* **2011**, *59*, 5881.
[42] M. Vashista, S. Paul, *Philos. Mag.* **2012**, *92*, 4194.
[43] I. C. Noyan, J. B. Cohen, *Residual Stress: Measurement by Diffraction and Interpretation*, Springer New York, NY **1987**.
[44] B. Putz, B. Völker, C. Semprimoschnig, M. J. Cordill, *Microelectron. Eng.* **2017**, *167*, 17.
[45] S. Kobayashi, *Rigaku J.* **2010**, *26*, 3.
[46] S. H. Oh, C. Rentenberger, J. Im, C. Motz, D. Kiener, H. P. Karnthaler, G. Dehm, *Scr. Mater.* **2011**, *65*, 456.
[47] B. Putz, G. Milassin, Y. V. Butenko, B. Voelker, C. Gammer, C. O. A. Semprimoschnig, M. J. Cordill, *Surf. Coat. Technol.* **2017**, *332*, 368.
[48] L. Astoreca, D. Schaubroeck, P. S. E. Tabaei, R. Ghobeira, M. O. de Beeck, R. Morent, H. D. Smet, N. D. Geyter, *Coatings* **2021**, *11*, 1352.
[49] M. J. Vasile, B. J. Bachman, *J. Vac. Sci. Technol., A* **1989**, *7*, 2992.
[50] R. L. Puurunen, W. Vandervorst, *J. Appl. Phys.* **2004**, *96*, 7686.

[51] R. L. Puurunen, W. Vandervorst, W. F. A. Besling, O. Richard, H. Bender, T. Conard, C. Zhao, A. Delabie, M. Caymax, S. D. Gendt, M. M. Heyns, M. Viitanen, M. de Ridder, H. H. Brongersma, Y. Tamminga, T. Dao, T. de Win, M. A. Verheijen, M. Kaiser, M. T. Tuominen, *J. Appl. Phys.* **2004**, *96*, 4878.
[52] H. C. Jansen, A. Sharma, K. Wieczerzak, G. K. Nayak, J. M. Schneider, J. J. Schwiedrzik, T. E. Edwards, J. Michler, *Scr. Mater.* **2025**, *260*, 116589.
[53] M. Collaud, S. H. Nowak, O. M. Küttel, P. Gröning, L. Schlapbach, *Appl. Surf. Sci.* **1993**, *72*, 19.
[54] S.-H. Li, W. Han, J. Li, E. Ma, Z. wei Shan, *Acta Mater.* **2017**, *126*, 202.
[55] W. D. Nix, *Metall. Trans. A* **1989**, *20*, 2217.
[56] E. O. Hall, *Proc. Phys. Soc. London, Sect. B* **1951**, *64*, 747.
[57] Z. C. Cordero, B. E. Knight, C. A. Schuh, *Int. Mater. Rev.* **2016**, *61*, 495.
[58] H. Elias, D. M. Hyde, *Am. J. Anat.* **1980**, *159*, 412.
[59] O. Kraft, P. A. Gruber, R. Mönig, D. Weygand, *Annu. Rev. Mater. Res.* **2010**, *40*, 293.
[60] Y. Leterrier, L. J. Medico, F. Demarco, J. E. Månson, U. Betz, M. F. Escolá, M. K. Olsson, F. Atamny, *Thin Solid Films* **2004**, *460*, 156.
[61] J. Wang, A. Misra, *Curr. Opin. Solid State Mater. Sci* **2011**, *15*, 20.
[62] O. Glushko, R. Pippan, D. Şopu, C. Mitterer, J. Eckert, *Nat. Commun.* **2024**, *15*, 5601.
[63] T. Jörg, M. J. Cordill, R. Franz, C. Kirchlechner, D. M. Többens, J. Winkler, C. Mitterer, *Mater. Sci. Eng., A* **2017**, *697*, 17.
[64] W. Cheng, E. Rossi, J. Bauer, J. P. Martins, R. Guillemet, L. Pethö, J. Michler, M. Sebastiani, *Acta Mater.* **2025**, *301*, 121474.
[65] E. Sortino, J. P. Houlton, J. C. Gertsch, O. D. Supekar, G. Skidmore, S. M. George, C. T. Rogers, V. M. Bright, *2019 20th International Conference on Solid-State Sensors, Actuators and Microsystems & Eurosensors XXXIII (TRANSDUCERS & EUROSENSORS XXXIII)*, IEEE, New York **2019**, 2404.
[66] A. A. Taylor, M. J. Cordill, L. Bowles, J. Schalko, G. Dehm, *Thin Solid Films* **2013**, *531*, 354.
[67] T. Li, Z. Y. Huang, Z. C. Xi, S. P. Lacour, S. Wagner, Z. Suo, *Mech. Mater.* **2005**, *37*, 261.
[68] O. Glushko, B. Putz, M. J. Cordill, *Thin Solid Films* **2020**, *699*, 137906.
[69] O. Glushko, P. Kraker, M. J. Cordill, *Appl. Phys. Lett.* **2017**, *110*, 191904.
[70] M. J. Cordill, A. Taylor, J. Schalko, G. Dehm, *Metall. Mater. Trans. A* **2010**, *41*, 870.
[71] D. Valdesueiro, G. M. Meesters, M. T. Kreutzer, J. R. van Ommen, *Materials* **2015**, *8*, 1249.
[72] S. Djaziri, D. Thiaudière, G. Geandier, P. O. Renault, E. L. Bourhis, P. Goudeau, O. Castelnau, D. Faurie, *Surf. Coat. Technol.* **2010**, *205*, 1420.
[73] T. Xie, T. E. J. Edwards, N. M. della Ventura, D. Casari, E. Huszár, L. Fu, L. Zhou, X. Maeder, J. J. Schwiedrzik, I. Utke, J. Michler, L. Pethö, *Thin Solid Films* **2020**, *711*, 138287.
[74] D. Toebbens, *J. Large-Scale Res. Facil.* **2016**, *2*, 1.
[75] S. Djaziri, D. Faurie, P. O. Renault, E. L. Bourhis, P. Goudeau, G. Geandier, D. Thiaudiere, *Acta Mater.* **2013**, *61*, 5067.
[76] C. O. W. Trost, Synchrotron Data Evaluation for BESSY-II (KMC-II): $\sin^2$ Analysis Toolkit, **2025**, https://zenodo.org/records/17349576.
[77] V. Hauk, *Structural and Residual Stress Analysis by Nondestructive Methods*, chapter 2.13 - X-ray elastic constants (XEC), 279, Elsevier Science B.V., Amsterdam **1997**.
[78] H. Wern, N. Koch, T. Maas, In *Residual Stresses VI, ECRS6*, volume 404 of *Materials Science Forum*. Trans Tech Publications Ltd, Switzerland **2002**, pp. 127–132.
[79] T. Chommaux, P. Renault, D. Thiaudiere, P. Godard, F. Paumier, T. Girardeau, S. Hurand, P. Goudeau, *Thin Solid Films* **2022**, *741*, 139035.
[80] C. O. W. Trost, Synchrotron Data Evaluation for BESSY-II (KMC-II): $\sin^2\psi$ Analysis Toolkit (Version v0.9) [Computer software], Zenodo, **2025**, https://doi.org/10.5281/ZENODO.17349576.